

# Impacts on Initial Condition Modification from Hyperspectral Infrared Sounding Data Assimilation: Comparisons between Full-Spectrum and Channel-Selection Scheme Based on Two-Month Experiments Using CrIS and IASI Observation

Qi Zhang

Center for Atmospheric Sciences, Hampton University, Hampton, Virginia, United States

Email: qi.zhang@hamptonu.edu

**How to cite this paper:** Zhang, Q. (2021) Impacts on Initial Condition Modification from Hyperspectral Infrared Sounding Data Assimilation: Comparisons between Full-Spectrum and Channel-Selection Scheme Based on Two-Month Experiments Using CrIS and IASI Observation. *International Journal of Geosciences*, 12, 763-783. <https://doi.org/10.4236/ijg.2021.129043>

**Received:** August 14, 2021

**Accepted:** September 10, 2021

**Published:** September 13, 2021

Copyright © 2021 by author(s) and Scientific Research Publishing Inc. This work is licensed under the Creative Commons Attribution International License (CC BY 4.0).

<http://creativecommons.org/licenses/by/4.0/>



Open Access

## Abstract

This paper discusses the performance difference between full-spectrum and channel-selection assimilation scheme of hyperspectral infrared observation, e.g. CrIS and IASI, on improving the accuracy of initial condition in numerical weather prediction. To accomplish this, we develop a 3D-Variational data assimilation system whose observation operator is a principal-component based fast radiative transfer model, which equips the direct assimilation of full-channel radiance from hyperspectral infrared sounders with high computational efficiency. This project's primary goal is to demonstrate that assimilation of infrared observation in a full-channel mode could improve the accuracy of initial condition compared to selected-channel assimilation. Results show that full-channel assimilation performs better than selected-channel assimilation in modifying low and middle troposphere (1000 - 700 hPa, 700 - 400 hPa) temperature and water vapor field, while marginal improvements from temperature and water vapor field could be found over upper troposphere (400 - 100 hPa). This research also proves the feasibility of an alternative path to data assimilation for the full usage of hyperspectral infrared sounding observation in numerical weather prediction.

## Keywords

Hyperspectral Infrared, Remote Sensing, Data Assimilation, Performance Evaluation, Numerical Weather Prediction

## 1. Introduction

Weather forecasting centers have been assimilating atmospheric infrared remote sensing observations into their Numerical Weather Prediction (NWP) system since the High-Resolution Infrared Sounder (HIRS) went into operation [1]. Currently, infrared remote sensing observation, especially hyperspectral infrared sounding data from Atmospheric InfraRed Sounder(AIRS) [2] [3] [4] [5] [6], Infrared Atmospheric Sounding Interferometer (IASI) [7] [8] [9] [10], Cross-track Infrared Sounder (CrIS) [11] [12] [13] [14] accounts for 4.2% (10.1%) of the forecast error reduction in global NWP system in northern (southern) hemisphere [15]. The impact of hyperspectral infrared observation to NWP will forward to a higher level with the deployment and operational assimilation of a new generation of polar-orbiting or geostationary hyperspectral satellites, e.g. Infrared Atmospheric Sounding Interferometer New Generation (IASI-NG) [16], Meteosat Third Generation hyperspectral InfraRed Sounder (MTG-IRS) [17], Geostationary Interferometric Infrared Sounder (GIIRS) [18]. By far, the assimilation scheme of hyperspectral infrared data used by major numerical centers is still focusing on taking advantage of a subset of channel observations among the entire spectrum, also known as selected-channel [19] [20] [21] which inevitably renders the information content from full-spectrum observation. Even though assimilation of a subset channel observation can maintain the efficiency of NWP system as high as possible while minimizing the loss of effective observational information, it is undeniable that most of the operational NWP systems cannot take full advantage of the complete information gathered by hyperspectral infrared sensors, which virtually hinders the accuracy advancement in weather prediction. Recent studies [22] [23] have shown that the accuracy of initial condition can be further improved by adding new channel observations to the operational channel selection scheme, which provides proof for the hypothesis that full-channel assimilation of hyperspectral infrared observation is more helpful in improving initial condition's accuracy than selected-channel scheme.

To compare the differences between full-channel assimilation and selected-channel assimilation on improving temperature and water vapor field's accuracy in initial condition, a 3-Dimensional Variational (3-Dvar) data assimilation (DA) system using principal-component-based radiative transfer model, is developed. Experiments assimilating hyperspectral infrared data on a full-and selected-channel basis will be conducted using this system to uncover the reason for performance difference.

In the next sections, we discuss this question in the order listed below: in Method and Data section by introducing you to the components in our 3-Dvar data assimilation system and methods used in data assimilation performance evaluation. Hyperspectral observations used by the assimilation system and conventional observation used in performance evaluation are briefed in Data and Experiment Design section. In Results and Analysis section, we shall go over the details from performance evaluation and discover the reason that causes the dif-

ference between full-channel and selected-channel assimilation schemes. We will talk about the insufficiency in this research and our further plan in the Conclusion and Discussion section.

## 2. Method and Data

### 2.1. Background Error Covariance and Observational Error Covariance Calculation

It is widely accepted that the quality of background error covariance matrix (B Matrix) is crucial to every DA system, for its high relevance to NWP model's systematic error. Before conducting experiments, we calculate B Matrix from 12-hour and 36-hour lead-time forecasts valid at 00:00 UTC and 12:00 UTC from Global Forecast System (GFS) operated by National Centers for Environmental Prediction (NCEP) [24] in January and June from 2017 to 2019 using NMC method [25] [26]. With a horizontal resolution of  $1.25^\circ \times 1.25^\circ$  and a vertical resolution of 31 levels from 1000 hPa to 1 hPa, this B Matrix can properly represent the error in initial condition generated by forecast model. In this study, B Matrices for January and June are generated respectively, as a series of monthly-separated B Matrix can better describe the sub-seasonal systematic error from NWP model than a unified one. Unlike B Matrix, the DA system inherits observational error covariance matrix (R Matrix) from open-accessed 1D-Var assimilation package released by Numerical Weather Prediction (NWP) Satellite Application Facility (SAF) in European Organization for the Exploitation of Meteorological Satellites (EUMETSAT) [27]-[33]. This decision is made up for the reasons listed below: 1) observational error covariance matrix only comprises instrumental error and fast forward radiative transfer model error, and fast radiative transfer model error is relatively static compared to the error in NWP model; 2) instrumental error is supposed to be steady, as it is only related to instrument's operating and healthy status.

### 2.2. Cloud Detection and Quality Control

Even though several Data Assimilation (DA) systems have the capability of assimilating infrared channel observations if the weighting function peak pressure level is above diagnostic cloud height over overcast areas [32] [34] [35] [36], the vertical resolution of GFS data used in this research is not sufficient enough to precisely diagnose cloud top height. Therefore, all experiments in this article will not assimilate any infrared observation over cloudy regions. To separate clear sky observation from cloudy ones, a cloud detection algorithm using equivalent cloud-top height and equivalent cloud cover calculated from the minimum residual method [37] is embedded in quality control process: if the equivalent cloud top height for an observation is above 700 hPa or the equivalent cloud cover is above 20%, cloud detection process will mark this observation as cloud-contaminated and reject it from data assimilation system.

The DA system used in the coming experiments runs a two-step quality control process to ensure the quality of observations before they are assimilated into initial condition. In the first step, Degree of information Freedom for Signal (*DFS*) [38] is calculated from following function:

$$DFS = H'_{(x)} \cdot B \cdot \left( H'_{(x)} \right)^T \cdot \left[ H'_{(x)} \cdot B \cdot \left( H'_{(x)} \right)^T + R \right]^{-1} \quad (1)$$

where  $H'$  is the Jacobian of fast forward radiative transfer model regarding initial condition  $x$ ,  $R$  ( $B$ ) is the background (observational) error covariance matrix, operator  $T$  stands for matrix transpose and operator  $\cdot$  refers to dot production. Once finishing Equation (1) calculation, DA system initiates a channel screening process: if a channel observation's value is smaller than 0.2, system will mark this observation as unqualified and discard it from data ingestion list. Based on the results from first step, the second step starts by calculating absolute brightness temperature difference between observation and simulation from initial condition. In this step, DA system eliminates the channel observation with an absolute difference larger than 1.0 K.

### 2.3. Minimization Algorithm

The primary function of a DA system is to determine the best estimation of initial condition ( $x$ ) by minimizing the cost function based on quality-controlled observation [39] [40] [41] [42] listed below:

$$J_{(x)} = \frac{1}{2} (x - x_b)^T \cdot B^{-1} \cdot (x - x_b) + \frac{1}{2} (y - H_{(x)})^T \cdot R^{-1} \cdot (y - H_{(x)}) \quad (2)$$

where  $H$  is a PC-based fast forward radiative transfer model which calculates simulated brightness temperature (BT) from initial condition. To find the minimum of  $J$ , DA system updates initial condition at each iteration ( $n+1$ ) using the equations below (Rodgers 1976, 2000):

$$x_{n+1} = x_b + U^{-1} \cdot V \quad (3)$$

$$U = B^{-1} + \left[ H'_{(x_n)} \right]^T \cdot R^{-1} \cdot H'_{(x_n)} \quad (4)$$

$$V = \left[ H'_{(x_n)} \right]^T \cdot R^{-1} \cdot \left[ (y - H_{(x_n)}) + H'_{(x_n)} \cdot (x_n - x_b) \right] \quad (5)$$

where  $n$  stands for iteration steps. In this system, Havemann-Taylor Fast Radiative Transfer Code (HT-FRTC) [43] [44] is used to calculate  $H$  and  $H'$ , for that Principal-Component-based fast forward model is more computationally effective than other fast forward radiative transfer models, e.g. Radiative Transfer for TOVS (RTTOV) [45] [46] and Community Radiative Transfer Model (CRTM) [47]. Besides, the precision of HTFRTC is comparable to RTTOV and CRTM [48] in simulating full-spectrum hyperspectral infrared radiance or brightness temperature.

### 2.4. Performance Evaluation

Mean Bias ( $MB$ ) and Standard Deviation ( $SD$ ) are the major variables in eva-

luating the quality of initial condition before and after assimilating hyperspectral infrared observation, which are widely used among various subjects [49]:

$$MB = \left( \sum_{n=1}^N (x - OBS) \right) / N \quad (6)$$

$$SD = \text{sqrt} \left( \sum_{n=1}^N [(x - OBS) - MB]^2 / N \right) \quad (7)$$

where *OBS* refers to conventional observations gathered by aircraft, ships, weather balloons, and surface stations. Statistically, mean bias is good at representing systematic bias and standard deviation is highly related to random bias.

## 2.5. Data

By far, there are four types of hyperspectral infrared Michelson interferometer operating on different polar-orbiting satellites: Atmospheric Sounding Interferometer (IASI) [50], Cross-track Infrared Sounder (CrIS) [51], Russian advanced infrared atmospheric sounder (IKFS-2) [52], Hyperspectral Infrared Atmospheric Sounder (HIRAS) [53]. Among these instruments, observations from CrIS and IASI are more widely accepted and used by operational NWP centers until a recent successful attempt on assimilating IKFS-2 observation into ECMWF's operational NWP system [54]. For this reason, experiments in this article only accept observations from IASI and CrIS instruments, which can be downloaded from NOAA Comprehensive Large Array-data Stewardship System (CLASS). Before initializing the DA system, the radiance observations are converted from radiance space to brightness temperature space: although the public has already accepted the concept that using radiance can improve data assimilation system's accuracy, as instrumental noise is more constant in radiance space, using brightness temperature can help DA system overcome slow convergence problem while minimizing the cost function and thus increase computational efficiency because brightness temperature space is more linear than radiance space. 12-hour lead time forecast products from GFS in January and June 2020 valid at 00:00 UTC and 12:00 UTC will provide initial condition for the DA system since B Matrix is derived from historical GFS data. In performance evaluation, temperature and water vapor observation from radiosonde, Aircraft Meteorological Data Reports (AMDAR), ship, and surface station [55] will help to quantify performance differences among upcoming experiments.

## 3. Experiment Design

As is shown in **Figure 1**, DA system will not take any observation from a Long-Wave InfraRed (LWIR) or Mid-Wave InfraRed (MWIR) channel if this channel is sensitive to the constituents listed below: O<sub>3</sub>, N<sub>2</sub>O, SO<sub>2</sub>, CH<sub>4</sub>, CFC-11, and CFC-12, due to the shortage of chemical information in GFS forecast product. Moreover, Short-Wave InfraRed (SWIR) observations are neglected because solar radiation may affect observation in SWIR spectrum range. Channel amount

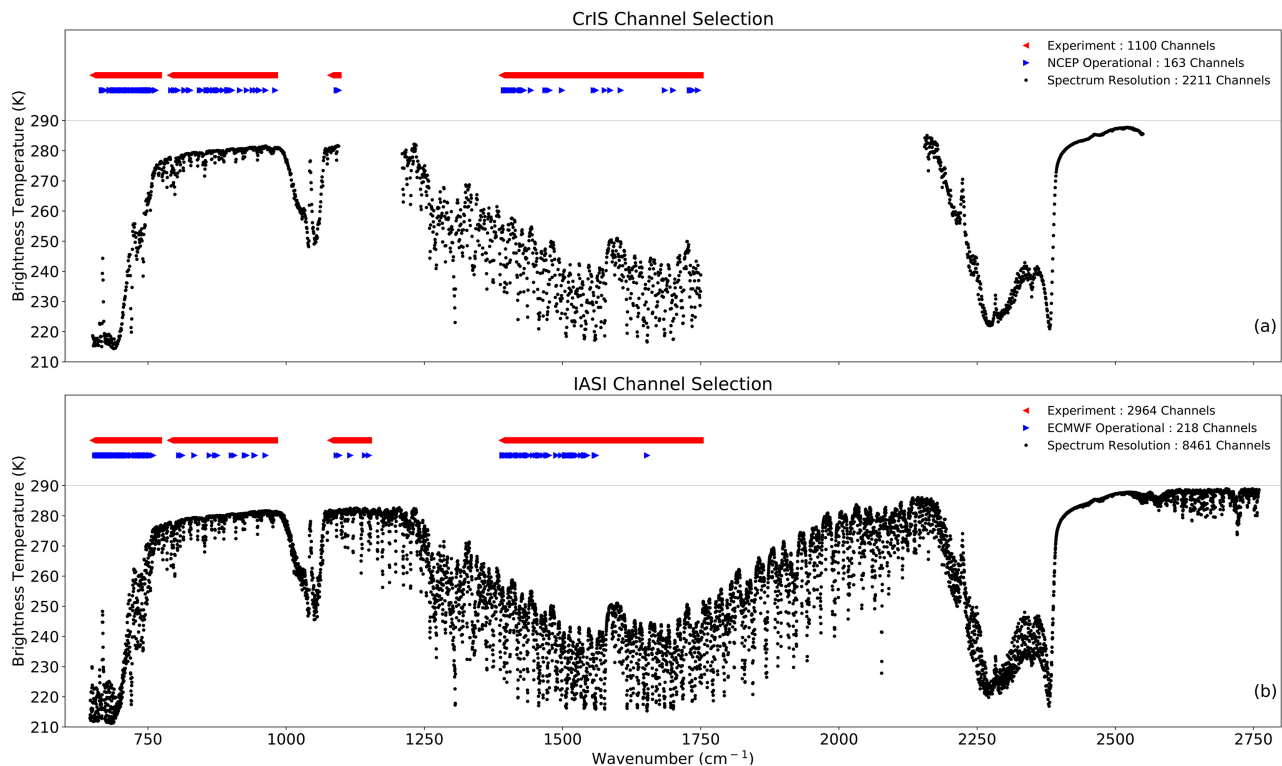


**Figure 1.** Channel observation used in FullChannel experiment (red triangle) and SelectedChannel (blue triangle) before quality control in CrIS (a) and IASI (b) instrument.

difference between full-channel assimilation (FullChannel) experiment and selected-channel assimilation (SelectedChannel) experiment is listed in **Table 1**. To make sure that results from CrIS data assimilation and IASI data assimilation are relatively comparable, observations with channel wavenumber larger than  $1750\text{ cm}^{-1}$  in IASI MWIR range are not used in the following experiments. In FullChannel experiments, DA process shall initialize with observations that meet the requirements mentioned in Cloud detection and quality control section. Unlike FullChannel experiment, a channel selection scheme is added to DA system between quality control and minimization process in SelectedChannel experiment. For CrIS data, a channel observation cannot obtain access to DA system if this channel is not included in the NCEP channel selection list [21]. The same is true for IASI observation, but this time, the channel selection scheme uses the ECMWF channel selection list [20] instead of NCEP. A detailed description of workflow for FullChannel and SelectedChannel experiment can be found in **Figure 2**.

## 4. Results and Analysis

### 4.1. CrIS Experiments

Before starting the experiments, we need to establish comprehensions of the spatial intersection between CrIS data coverage and conventional observation. As can be seen in **Figure 3**, around 00:00 (23:30-00:30) UTC and 12:00 (11:30-12:30)

UTC, CrIS observation mainly covers the area from 45°W to 45°E and from 135°E to 135°W. In the CrIS data coverage area, most conventional observations locate in Europe, South Africa, Central Pacific, and Alaska. In marine region, the amount of conventional observation is far less than that over land in January (Figure 3(a)), this situation intensifies significantly in June (Figure 3(b)).

Table 1. Detailed CrIS and IASI channel usage in each experiment.

Channel Range		LWIR Channels				MWIR Channels	
		CO <sub>2</sub>		Atmospheric Window		H <sub>2</sub> O	
Experiment Name		Full Channel	Selected Channel	Full Channel	Selected Channel	Full Channel	Selected Channel
Channel	CrIS	193	78	330	48	577	37
Amount	IASI	481	121	1042	19	1441	78

### Experiment Workflow

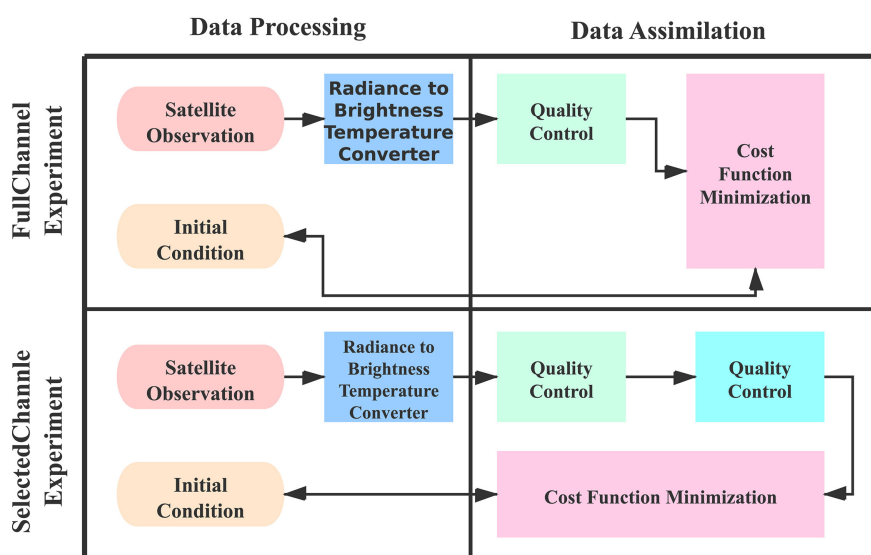


Figure 2. Experiment workflow for FullChannel and SelectedChannel experiment.

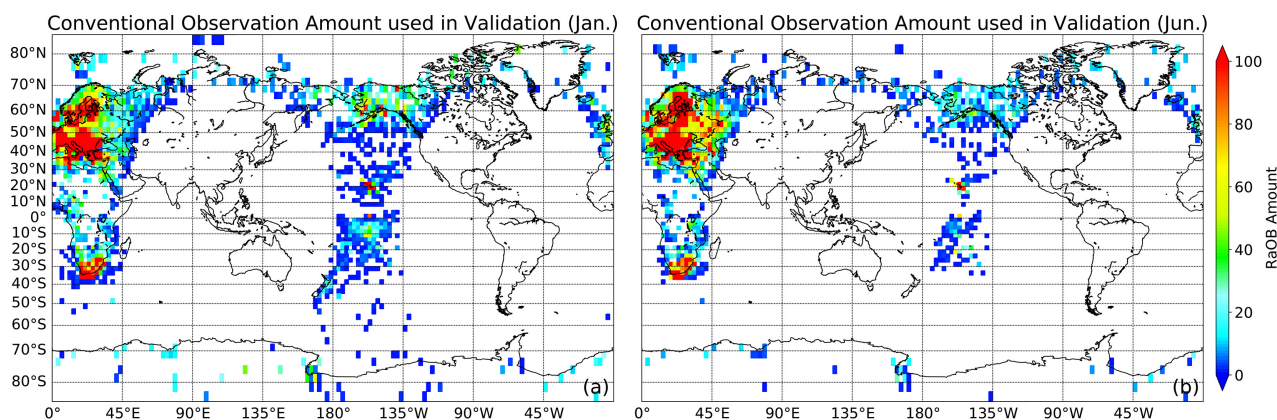
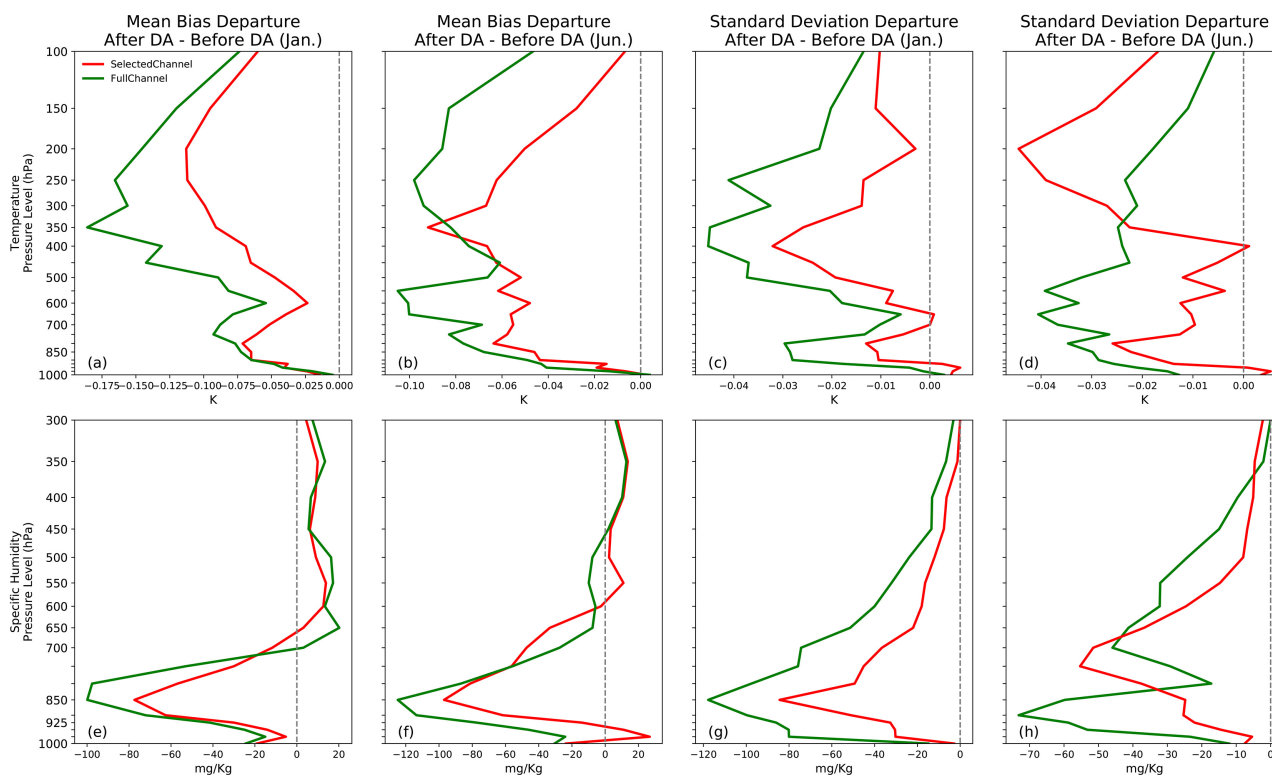


Figure 3. Spatial distribution of conventional observation used in performance evaluation located within CrIS observation coverage in January (a) and June (b).

By comparing temperature mean bias departure profile from FullChannel experiment (green line) and SelectedChannel (red line) experiment in January (**Figure 4(a)**), full-channel assimilation method holds a better skill in reducing systematic error (mean bias) in initial condition than selected-channel assimilation in middle troposphere (700 - 400 hPa) and upper troposphere (400 - 100 hPa). On average, temperature mean bias reduction in FullChannel experiment against SelectedChannel experiment is 0.046 K in middle troposphere and 0.048 K in upper troposphere, but this improvement shrinks to 0.005 K in low troposphere (1000 - 700 hPa). Situations in June (**Figure 4(b)**) are fairly the same as January, except for a few changes: FullChannel experiment's improvement against SelectedChannel experiment drops to 0.028 K in middle troposphere and 0.026 K in upper troposphere, while an additional 0.008 K performance increase can be found in low troposphere compared to January. From the results shown in **Figure 4(c)** and **Figure 4(d)**, both full-channel and selected-channel assimilation methods can reduce the temperature field's random error (standard deviation) in initial condition, but the magnitude of improvement is different. In low troposphere, FullChannel experiment is ahead of SelectedChannel experiment by 0.012 K in January and 0.014 K in June, this precedence continues to exist in middle troposphere with a slight magnitude change: 0.011 K in January and 0.025 K in June. Performance of FullChannel experiment is still in the lead (0.015 K) in January over upper troposphere, but get surpassed by SelectedChannel experiment in June with a 0.0064 K decrease. Results from **Figure 4(e)** and **Figure 4(f)** illustrate that most of the improvements that water vapor field receives from hyperspectral IR data assimilation locate in low troposphere and full-channel assimilation method eliminates another 13.17 mg/kg (27.02 mg/kg) from mean bias in January (June) regarding selected-channel assimilation method, while neutral and negative impact can be detected in middle and upper troposphere. Although no positive impact arises after assimilating hyperspectral IR observation in middle and upper troposphere, uncertainty in full-channel assimilation method's performance enhancement makes the conclusion more unpredictable: in January, FullChannel experiment lags SelectedChannel experiment by 5.56 mg/kg in middle troposphere and 3.25 mg/kg in upper troposphere; but in June, FullChannel experiment is in the lead with 1.98 mg/kg in middle troposphere and 0.95 mg/kg in upper troposphere. Both FullChannel and SelectedChannel experiment contributes positive impact on random error cancellation to water vapor field, according to **Figure 4(g)** and **Figure 4(h)**. With an extra 40.29 mg/kg (14.32 mg/kg) improvement in January (June) within low troposphere, full-channel assimilation method seizes a higher performance compared to selected-channel assimilation method, and so is in middle troposphere, where FullChannel experiment's improvement over SelectedChannel experiment is 16.96 mg/kg in January and 10.77 mg/kg in June in an average scale. Different from the results in low and middle troposphere, full-channel assimilation method experiences an upper-troposphere performance degradation in June, as SelectedChannel experiment exceeds FullChannel experiment by 2.37 mg/kg.



**Figure 4.** Mean Bias and Standard Deviation departure (after CrIS DA - Before DA) for temperature and water vapor field in January (a, c, e, g) and June (b, d, f, h).

Profiles in **Figure 4** demonstrate hyperspectral IR data assimilation's impact on improving temperature and water vapor field's accuracy in initial condition as well as full-channel assimilation's performance enhancement over selected-channel assimilation in spatial average scale. Still, regional performance difference between full-channel and selected-channel assimilation methods remains uncertain. To disclose this, we calculate the standard deviation in a  $7.5^\circ \times 7.5^\circ$  horizontal resolution by organizing conventional observation and initial condition (before and after data assimilation) to the same projection. **Figure 5** shows the spatial distribution standard deviation departure between FullChannel and SelectedChannel experiment in integral (a), low (b), middle (c), and upper (d) troposphere. In **Figure 5(a)**, FullChannel experiment suffers from performance decrease in high latitude region ( $60^\circ\text{N} - 90^\circ\text{N}$  and  $60^\circ\text{S} - 90^\circ\text{S}$ ) comparing to SelectedChannel experiment, this symptom may result from underestimation of surface skin temperature in initial condition [56]. Due to a lack of conventional observation, FullChannel experiment suffers from a performance decrease in central and northern Africa. Beneath 400 hPa in mid-latitude region, standard deviation in FullChannel experiment is approximately 0.01 K higher than that in SelectedChannel experiment, comparing to SelectedChannel experiment. On account of conventional observation shortage in upper troposphere, the spatial variation of standard deviation departure is relatively higher than the other parts in the troposphere. But in southern and western Europe, where the observation

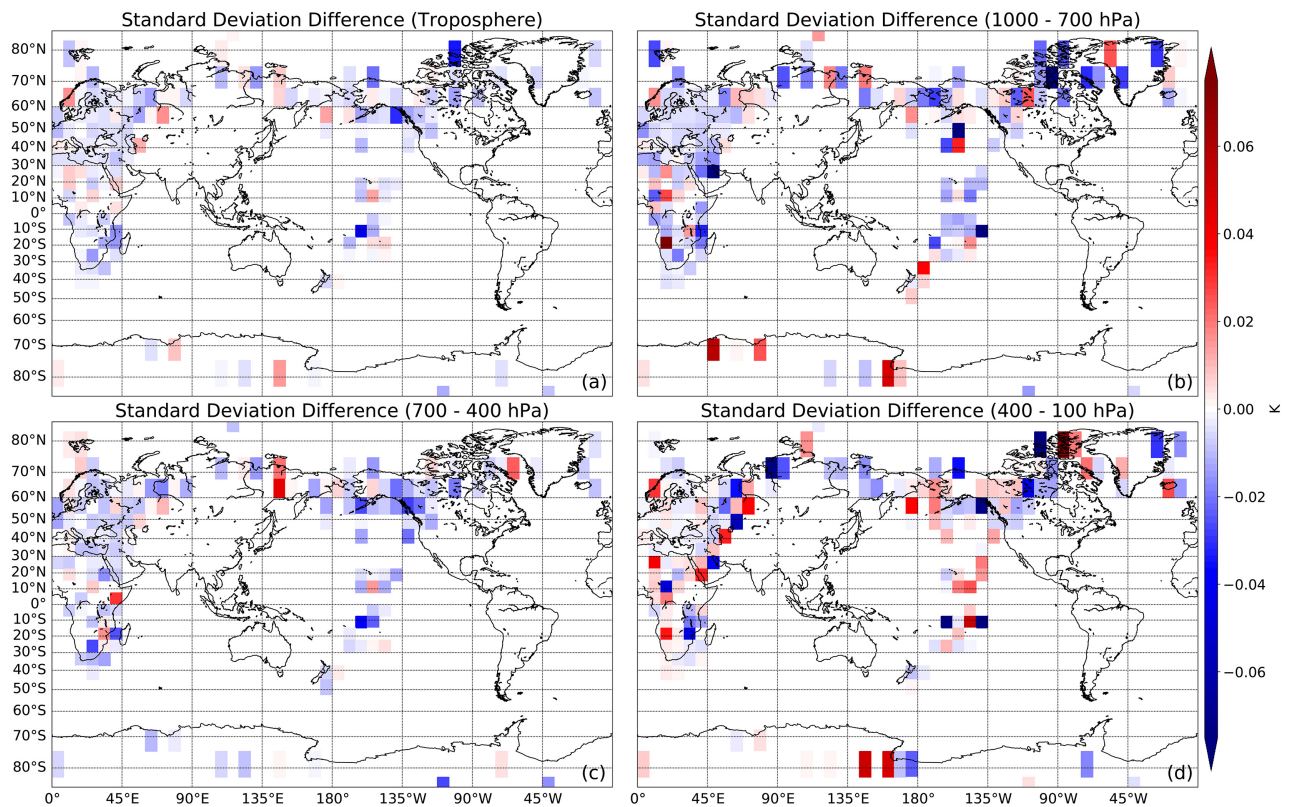


**Figure 5.** Spatial distribution of temperature standard deviation departure (FullChannel - SelectedChannel) after CrIS DA in integral (a), low (b), middle (c), upper (d) troposphere.

amount is the highest, marginal enhancement from FullChannel experiment in reducing standard deviation continues persisting. In **Figure 6**, the spatial distribution of water vapor standard deviation departure is calculated using the same approach as is used in **Figure 5**. The result in **Figure 6(a)** shows that performance deficiency in full-channel assimilation over high latitudes (compared to selected-channel assimilation) still exist in the water vapor field, but in low (**Figure 6(b)**) and middle troposphere (**Figure 6(c)**), symptom alleviates remarkably compared to the situation in upper troposphere (**Figure 6(d)**). Meanwhile, in areas where a sizeable amount of conventional observation locates, e.g. Europe, the performance of FullChannel experiment is always in the lead.

From the results listed above, we can conclude that: 1) both full-channel and selected-channel assimilation method can improve the accuracy of initial condition by reducing temperature field's systematic and random error, together with the random error in water vapor field; 2) generally, the performance of full-channel assimilation overpasses selected-channel assimilation in correcting low and middle troposphere temperature and water vapor field. To find the reason for the conclusions, we calculate the weighting function and DFS for each channel used in FullChannel experiment based on the average atmospheric variable profile from ECMWF [57]. By comparing the DFS for temperature (**Figure 7(a)**) and water vapor (**Figure 7(b)**) of each channel used in FullChannel experiment (dots) and SelectedChannel experiment (the dots that shares the same

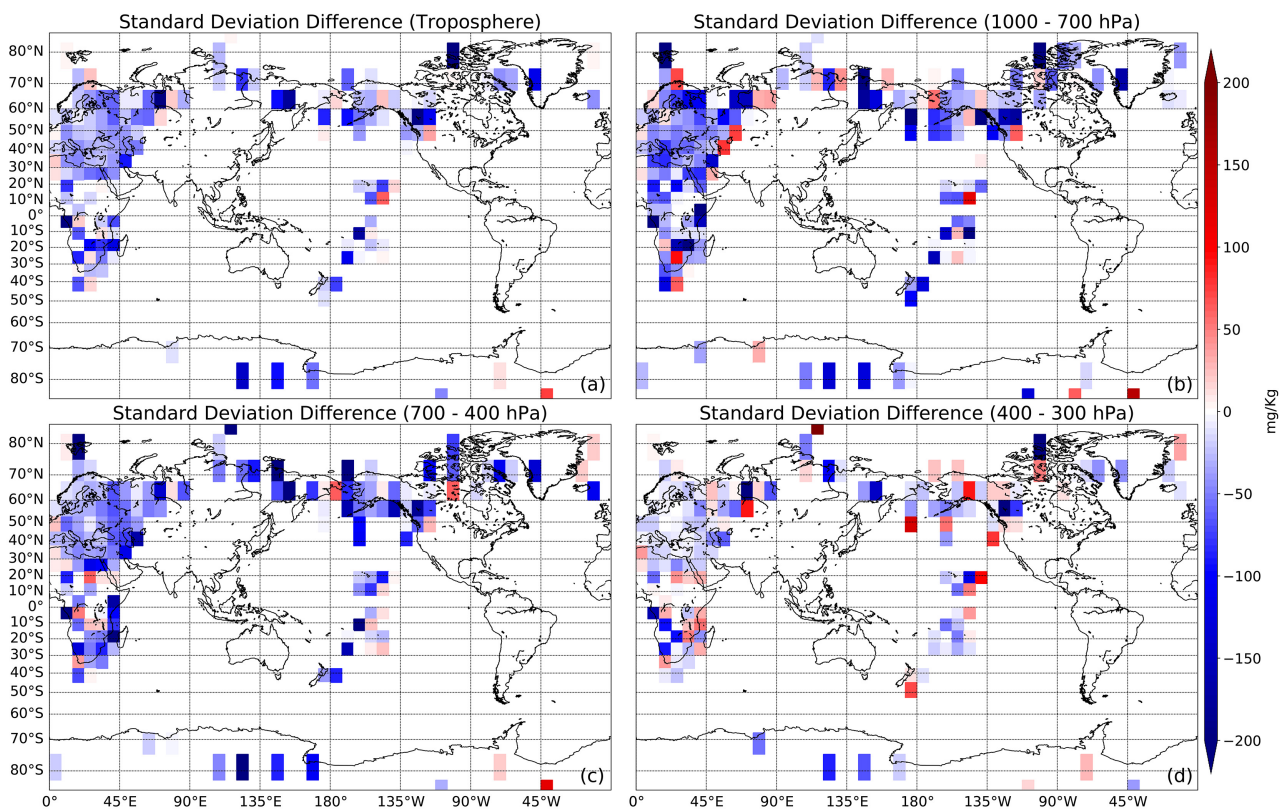


**Figure 6.** Spatial distribution of water vapor standard deviation departure (FullChannel - SelectedChannel) after CrIS data assimilation in integral (a), low (b), middle (c), upper (d) troposphere.

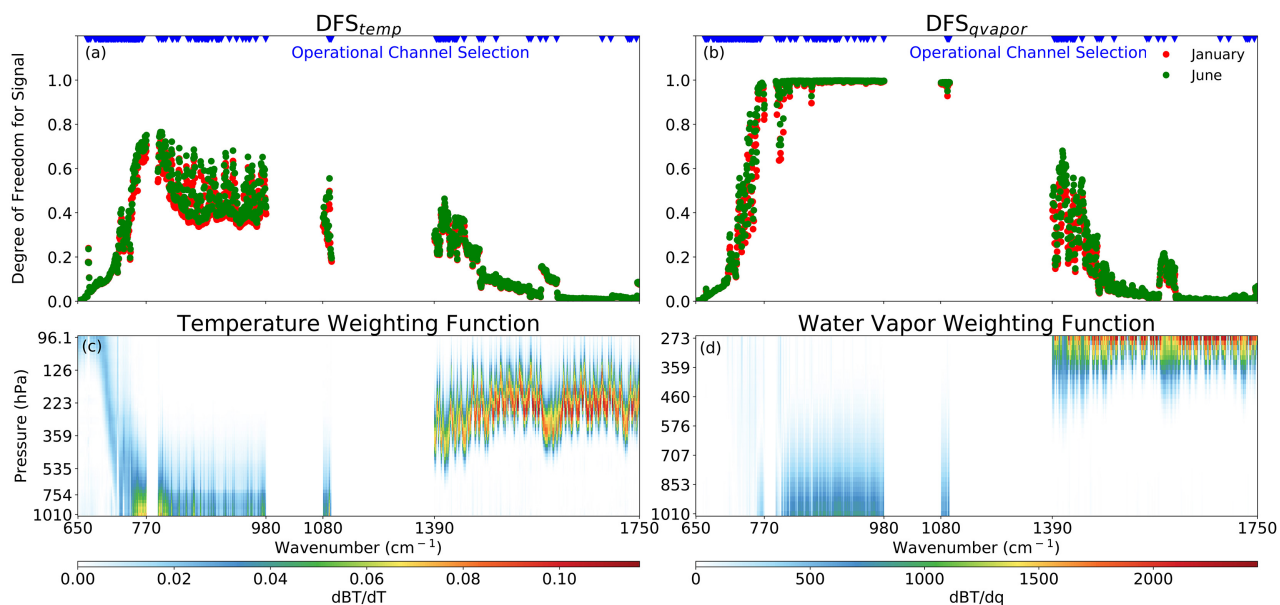


**Figure 7.** DFS for temperature (a) and water vapor (b) of each CrIS Channel shown in **Figure 1(a)** and their weighting function to temperature (c) and water vapor (d).

wavenumber with blue triangles), we could find out that the DFS for channels used in selected-channel assimilation is always higher than 0.1 and most of these channels are assimilated in both FullChannel and SelectedChannel experiment,

while some of these channels will be discarded by quality control process in the DA system. In addition to the channels used in SelectedChannel experiment, FullChannel experiment also assimilates other channels rejected by channel selection scheme whose DFS is normally higher than 0.38, and a considerably large amount of them are located in LWIR region, especially atmospheric window bands. Plus, weighting function peak pressure level in **Figure 7(c)** and **Figure 7(d)** indicates that these additional channels assimilated in FullChannel experiment are partial to modify temperature and water vapor field in low and middle troposphere. This could explain why improvement from full-channel assimilation locate in middle and low troposphere: as so many high-DFS channels carrying useful temperature and water vapor information in middle and low troposphere are assimilated by DA system, modified initial condition from FullChannel experiment is supposed to have a better performance than SelectedChannel experiment in middle and low troposphere.

## 4.2. IASI Experiments

To validate the conclusions drawn from CrIS experiments Section, supplementary experiments that assimilate IASI data are conducted in this section. From the spatial distribution of conventional observations amount in **Figure 8**, what we can confirm is most observations are located along the coastal area in far east Asia, eastern Australia, Brazil, and southern England. Amount-wise, observations used in evaluating initial condition's accuracy after IASI assimilation are not as sufficient as are used in CrIS Experiments, as the maximum observation amount within a  $2.5^\circ \times 2.5^\circ$  grid is around 100, while this amount can be as high as 200 in CrIS experiment results evaluation. Thus, results from IASI data experiment and CrIS data assimilation may slightly differ from each other.

Profiles in **Figure 9** presents the mean bias and standard deviation departure in initial condition between FullChannel and SelectedChannel experiment after assimilating IASI observation. In low troposphere, temperature field accuracy from FullChannel experiment is higher than SelectedChannel experiment, as the mean bias from FullChannel experiment is 0.005 K (0.009 K) smaller than SelectedChannel experiment in January (June) and the standard deviation is 0.012 K (0.014 K) smaller respectively. Below 850 hPa, full-channel assimilation experiences an accuracy loss on mean bias reduction (**Figure 9(a)** and **Figure 9(b)**), but it still keeps high proficiency on standard deviation reduction throughout low troposphere. FullChannel experiment's mean bias (0.074 K in January and 0.077 K in June) and standard deviation (0.025 K in January and 0.018 K in June) improvements against SelectedChannel experiment in middle troposphere indicate full-channel assimilation is better at diminishing temperature error in initial condition than selected-channel assimilation method, so is in the upper troposphere, where the additional mean bias (standard deviation) reduction is 0.041 K (0.037 K) in January and 0.053 K (0.042 K) in June. In the water vapor field, most of the positive impact concentrates in low and middle troposphere. In January, FullChannel experiment obtains 5.73 mg/kg (12.06 mg/kg) mean bias

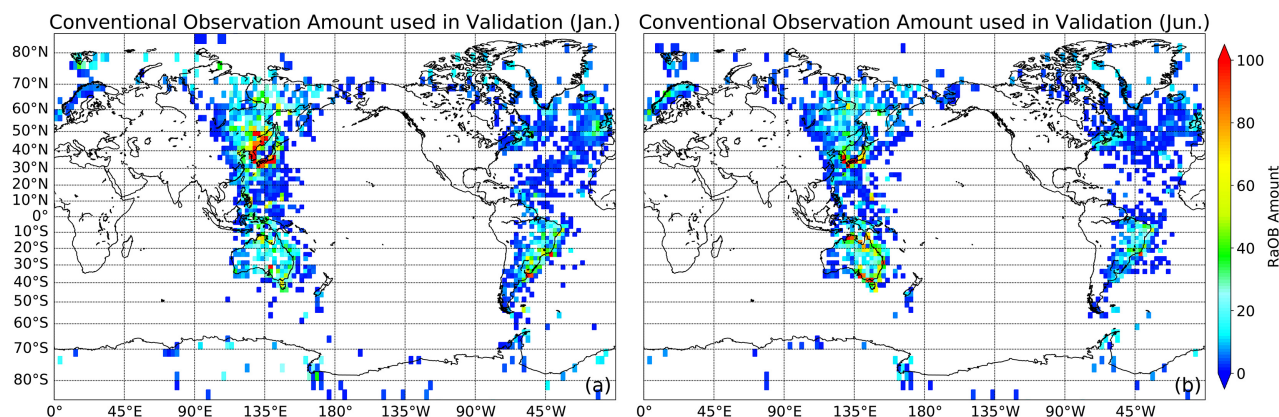


**Figure 8.** Spatial distribution of conventional observation used in performance evaluation located within IASI observation coverage in January (a) and June (b).

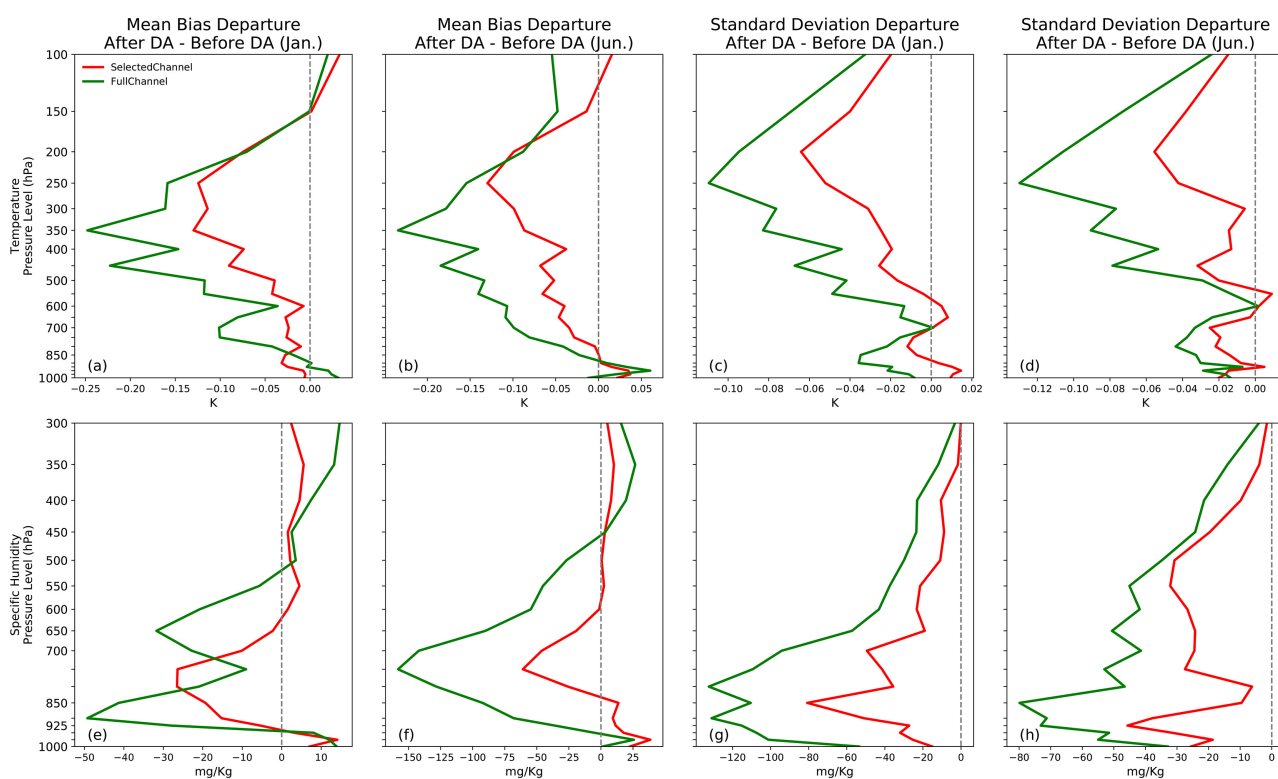


**Figure 9.** Mean Bias and Standard Deviation departure (after IASI DA - Before DA) for temperature and water vapor field in January (a, c, e, g) and June (b, d, f, h).

decrease in low (middle) troposphere over SelectedChannel experiment, but this number drops to  $-7.62$  mg/kg in upper troposphere. The same situation happens in June as well, but with a subtle magnitude change:  $45.93$  mg/kg ( $48.13$  mg/kg) decrease against SelectedChannel in low (middle) troposphere and  $12.95$  mg/kg increase in upper troposphere. Unlike the negative impact from IASI assimilation in mean bias reduction over upper troposphere, FullChannel experiments can diminish water vapor standard deviation more effectively than SelectedChannel experiment. Same as mean bias, most of the standard deviation im-

provement from full-channel assimilation concerning selected-channel assimilation stays in low and middle troposphere, while only marginal improvements can be detected in upper troposphere: in January, 40.39 mg/kg (16.94 mg/kg) improvements are found in low (middle) troposphere, but only 8.64 mg/kg improvement locates in upper troposphere; even though the magnitude levels up to 9.08 mg/kg in June in upper troposphere, it still falls behind low and middle-level improvement (32.58 mg/kg and 15.32 mg/kg).

Results from standard deviation departure between full-channel and selected-channel assimilation of IASI data share the same conclusion with CrIS experiments: 1) performance of full-channel assimilation over high latitude area is lower than selected-channel assimilation (**Figure 10(a)**); 2) most of the mid-latitude performance degradation in full-channel assimilation occurs in low troposphere over East Asia (**Figure 10(b)**), but this phenomenon alleviates in middle troposphere (**Figure 10(c)**) and upper troposphere (**Figure 10(d)**). **Figure 11** shows the spatial distribution of water vapor standard deviation departure between FullChannel and SelectedChannel experiment, From which we can conclude: 1) standard deviation from FullChannel experiment is lower than SelectedChannel in the areas with accumulated observation amount larger than 20; 2) latitude-related performance variation is highly detectable in low troposphere than the other level in the troposphere.

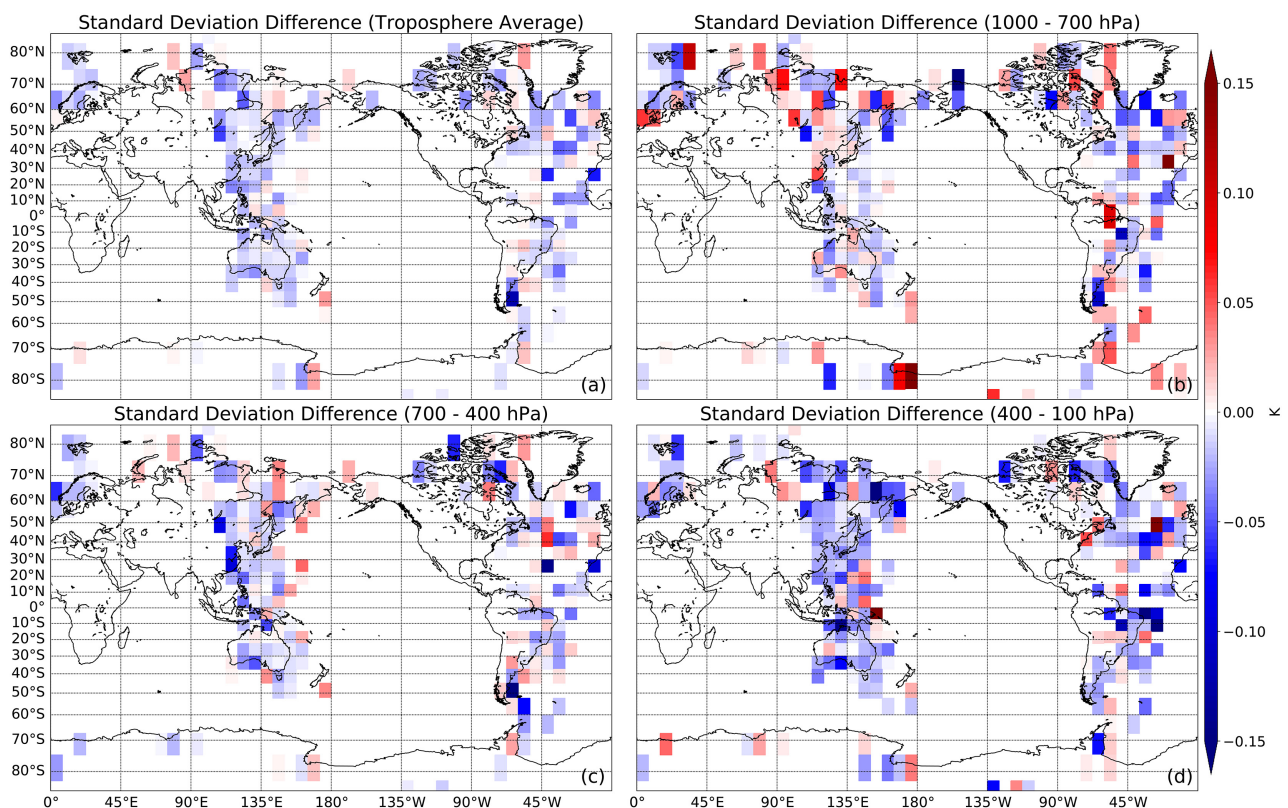


**Figure 10.** Spatial distribution of temperature standard deviation departure (FullChannel - SelectedChannel) after IASI DA in integral (a), low (b), middle (c), upper (d) troposphere.

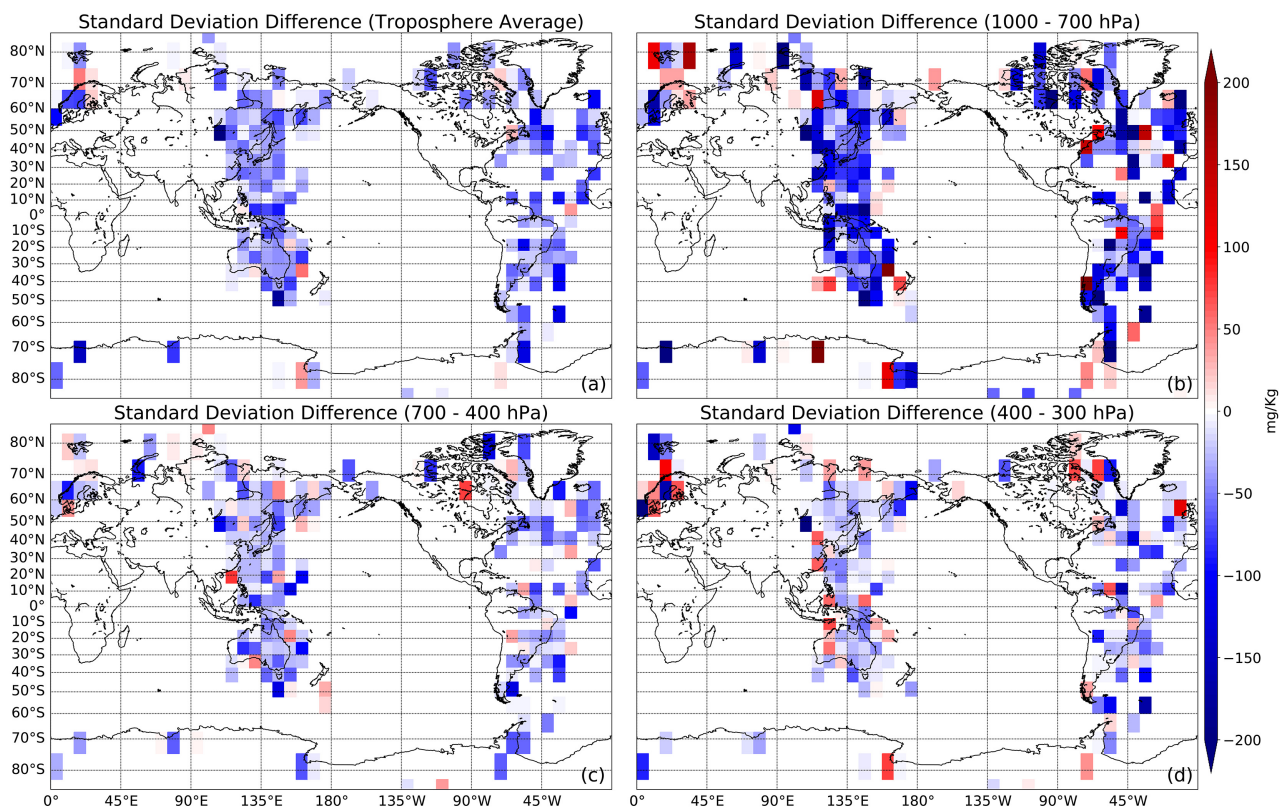


**Figure 11.** Spatial distribution of water vapor standard deviation departure (FullChannel - SelectedChannel) after IASI data assimilation in integral (a), low (b), middle (c), upper (d) troposphere.

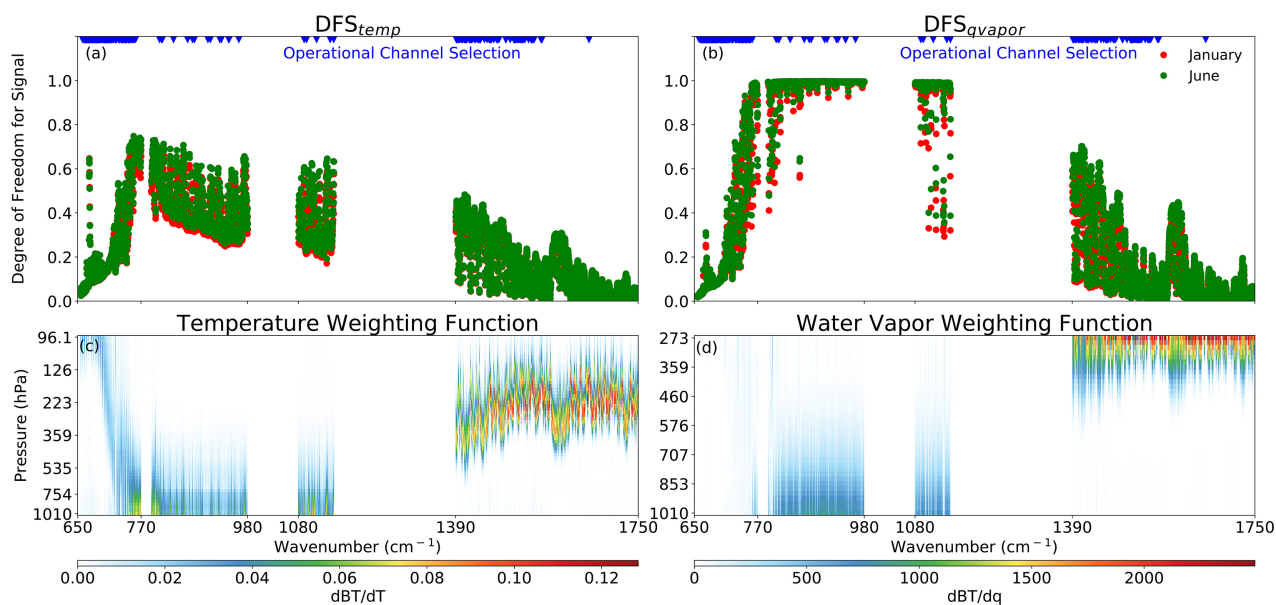


**Figure 12.** DFS for temperature (a) and water vapor (b) of each IASI Channel shown in **Figure 1(a)** and their weighting function to temperature (c) and water vapor (d).

Based on the results listed above, it is straightforward to conclude that both full-channel and selected-channel assimilation method can improve the accuracy of temperature and water vapor field in initial condition, and full-channel assi-

milation method is more skillful than selected-channel at reducing initial condition's systematic and random error in low and middle troposphere. Furthermore, evidence from DFS value and weighting function peak pressure level of each channel used in IASI data assimilation showed in **Figure 12** are in accordance with the ones disclosed in **Figure 7**, which provides effective supplementary proof that atmospheric window channels in hyperspectral IR observation can help data assimilation system improve temperature and water vapor field's accuracy in initial condition.

## 5. Discussion and Conclusion

From full-channel and selected-channel assimilation experiments using CrIS and IASI observation, we can extract the conclusions listed below: both full-channel and selected-channel assimilation methods are skilled at improving the quality of temperature and water vapor field in initial condition, but the improvement from full-channel assimilation method is more distinguishable than selected-channel method; performance improvement in full-channel assimilation may due to the increase of high DFS value ( $\geq 0.2$ ) channel usage in the data assimilation process, especially the atmospheric window channels in LWIR region, especially atmospheric window channels, whose weighing function peak pressure level mostly located in low and middle troposphere. In terms of computational efficiency, all experiments in this article are conducted using an 8-nodes Raspberry Pi 4B Single-Board Computer (SBC) cluster, which demonstrates that operational NWP centers can conduct full-channel assimilation of hyperspectral IR sounding observation as SBC Cluster's computational performance is far behind the HPC (High-Performance Computing) systems in NWP centers, and further improvements on temperature and water vapor field's accuracy in initial condition can be achieved if PC-based fast forward radiative transfer model can be used in DA system when assimilating hyperspectral IR observation.

Undisputedly, this research still faces a few shortcomings. For example, we are not capable of analyzing the seasonal performance variation in full-channel and selected-channel because all the experiments are conducted on a monthly basis. Nonetheless, experiments in this research reveal that full-channel assimilation method can reduce the initial condition's bias more effectively than the selected-channel method, further investigations are still needed to quantify the accuracy impacts on numerical weather prediction due to initial condition's bias reduction.

## Acknowledgements

The author is also grateful for the insightful comments offered by the anonymous peer reviewers. The generosity and expertise of one and all have improved this study in innumerable ways and saved me from many errors. Those that inevitably remain are entirely my own responsibility. Prof. William L. Smith Sr. from the Department of Atmospheric and Oceanic Sciences at the University of

Wisconsin—Madison provides valuable advises on hyperspectral infrared sounding observation quality control and bias correction.

### Conflicts of Interest

The author declares no conflicts of interest regarding the publication of this paper.

### References

- [1] Kelly, G.A.M., Mills, G.A. and Smith, W.L. (1978) Impact of Nimbus-6 Temperature Soundings on Australian Region forecasts. *Bulletin of the American Meteorological Society*, **59**, 393-406. <https://doi.org/10.1175/1520-0477-59.4.393>
- [2] Derber, J.C., Van Delst, P., Su, X., Li, X., Okamoto, K. and Treadon, R. (2003) Enhanced Use of Radiance Data in the NCEP Data Assimilation System. 13th *International TOVS Study Conference*, Adele, 15 October 2003, 1-8. [https://cimss.ssec.wisc.edu/itwg/itsc/itsc13/proceedings/session1/1\\_8\\_derber.pdf](https://cimss.ssec.wisc.edu/itwg/itsc/itsc13/proceedings/session1/1_8_derber.pdf)
- [3] McNally, A.P., Watts, P.D., Smith, A.J., Engelen, R., Kelly, G.A., Thépaut, J.N. and Matricardi, M. (2006) The Assimilation of AIRS radiance data at ECMWF. *Quarterly Journal of the Royal Meteorological Society*, **132**, 935-957. <https://doi.org/10.1256/qj.04.171>
- [4] Le Marshall, J., Jung, J., Derber, J., Chahine, M., Treadon, R., Lord, S.J., *et al.* (2006) Improving Global Analysis and Forecasting with AIRS. *Bulletin of the American Meteorological Society*, **87**, 891-894. <http://www.jstor.org/stable/26217190> <https://doi.org/10.1175/BAMS-87-7-891>
- [5] Pavelin, E.G., English, S.J. and Eyre, J.R. (2008) The Assimilation of Cloud-Affected Infrared Satellite Radiances for Numerical Weather Prediction. *Quarterly Journal of the Royal Meteorological Society*, **134**, 737-749. <https://doi.org/10.1002/qj.243>
- [6] Susskind, J. and Reale, O. (2010) Improving Forecast Skill by Assimilation of AIRS Temperature Soundings. 2010 *IEEE International Geoscience and Remote Sensing Symposium*, Honolulu, 25-30 July 2010, 3534-3537. <https://doi.org/10.1109/IGARSS.2010.5652458>
- [7] Hilton, F., Atkinson, N.C., English, S.J. and Eyre, J.R. (2009) Assimilation of IASI at the Met Office and Assessment of Its Impact through Observing System Experiments. *Quarterly Journal of the Royal Meteorological Society*, **135**, 495-505. <https://doi.org/10.1002/qj.379>
- [8] Collard, A.D. and McNally, A.P. (2009) The Assimilation of Infrared Atmospheric Sounding Interferometer Radiances at ECMWF. *Quarterly Journal of the Royal Meteorological Society*, **135**, 1044-1058. <https://doi.org/10.1002/qj.410>
- [9] Guidard, V., Fourrié, N., Brousseau, P. and Rabier, F. (2011) Impact of IASI Assimilation at Global and Convective Scales and Challenges for the Assimilation of Cloudy Scenes. *Quarterly Journal of the Royal Meteorological Society*, **137**, 1975-1987. <https://doi.org/10.1002/qj.928>
- [10] Randriamampianina, R., Iversen, T. and Storto, A. (2011) Exploring the Assimilation of IASI Radiances in Forecasting Polar Lows. *Quarterly Journal of the Royal Meteorological Society*, **137**, 1700-1715. <https://doi.org/10.1002/qj.838>
- [11] Collard, A., Derber, J., Treadon, R., Atkinson, N., Jung, J. and Garrett, K. (2012) Toward Assimilation of CrIS and ATMS in the NCEP Global Model. 18th *International TOVS Study Conferences*, Toulouse, 21-27 March 2012, 1-31. [https://library.ssec.wisc.edu/research\\_Resources/publications/pdfs/ITSC18/collard0](https://library.ssec.wisc.edu/research_Resources/publications/pdfs/ITSC18/collard0)

- [1\\_ITSC18\\_2012.pdf](#)
- [12] Eresmaa, R., Letertre-Danczak, J., Lupu, C., Bormann, N. and McNally, A.P. (2017) The Assimilation of Cross-Track Infrared Sounder Radiances at ECMWF. *Quarterly Journal of the Royal Meteorological Society*, **143**, 3177-3188. <https://doi.org/10.1002/qj.3171>
- [13] Wang, P., Li, J., Li, Z., Lim, A.H., Li, J., Schmit, T.J. and Goldberg, M.D. (2017) The Impact of Cross-Track Infrared Sounder (CrIS) Cloud-Cleared Radiances on Hurricane Joaquin (2015) and Matthew (2016) Forecasts. *Journal of Geophysical Research: Atmospheres*, **122**, 13201-13218. <https://doi.org/10.1002/2017JD027515>
- [14] Li, J., Wang, P., Han, H., Li, J. and Zheng, J. (2016) On the Assimilation of Satellite Sounder Data in Cloudy Skies in Numerical Weather Prediction Models. *Journal of Meteorological Research*, **30**, 169-182. <https://doi.org/10.1007/s13351-016-5114-2>
- [15] McNally, A. (2014) The Impact of Satellite Data on NWP. *ECMWF Seminar on Use of Satellite Observations in NWP*, Reading, United Kingdom, 8-12 September 2014, 1-10. <https://www.ecmwf.int/sites/default/files/elibrary/2015/11061-impact-satellite-data-nwp.pdf>
- [16] Crevoisier, C., Clerbaux, C., Guidard, V., Phulpin, T., Armante, R., Barret, B., *et al.* (2014) Towards IASI-New Generation (IASI-NG): Impact of Improved Spectral Resolution and Radiometric Noise on the Retrieval of Thermodynamic, Chemistry and Climate Variables. *Atmospheric Measurement Techniques*, **7**, 4367-4385. <https://doi.org/10.5194/amt-7-4367-2014>
- [17] Tjemkes, S., Gigli, S., Fowler, G. and Stuhlmann, R. (2015) The MTG-IRS Mission. *Proceedings of Fourier Transform Spectroscopy and Hyperspectral Imaging and Sounding of the Environment*, Santa Fe, 11-15 February 2007, Paper No. HW1B-2. <https://doi.org/10.1364/HISE.2015.HW1B.2>
- [18] Yang, J., Zhang, Z., Wei, C., Lu, F. and Guo, Q. (2017) Introducing the New Generation of Chinese Geostationary Weather Satellites, Fengyun-4. *Bulletin of the American Meteorological Society*, **98**, 1637-1658. <https://doi.org/10.1175/BAMS-D-16-0065.1>
- [19] Rabier, F., Fourrié, N., Chafäi, D. and Prunet, P. (2002) Channel Selection Methods for Infrared Atmospheric Sounding Interferometer Radiances. *Quarterly Journal of the Royal Meteorological Society*, **128**, 1011-1027. <https://doi.org/10.1256/0035900021643638>
- [20] Collard, A.D. (2007) Selection of IASI Channels for Use in Numerical Weather Prediction. *Quarterly Journal of the Royal Meteorological Society*, **133**, 1977-1991. <https://doi.org/10.1002/qj.178>
- [21] Gambacorta, A. and Barnet, C.D. (2012) Methodology and Information Content of the NOAA NESDIS Operational Channel Selection for the Cross-Track Infrared Sounder (CrIS). *IEEE Transactions on Geoscience and Remote Sensing*, **51**, 3207-3216. <https://doi.org/10.1109/TGRS.2012.2220369>
- [22] Ventress, L. and Dudhia, A. (2014) Improving the Selection of IASI Channels for Use in Numerical Weather Prediction. *Quarterly Journal of the Royal Meteorological Society*, **140**, 2111-2118. <https://doi.org/10.1002/qj.2280>
- [23] Smith, W.L., Zhang, Q., Shao, M. and Weisz, E. (2020) Improved Severe Weather Forecasts Using LEO and GEO Satellite Soundings. *Journal of Atmospheric and Oceanic Technology*, **37**, 1203-1218. <https://doi.org/10.1175/JTECH-D-19-0158.1>
- [24] National Centers for Environmental Prediction/National Weather Service/NOAA/U.S. Department of Commerce (2007) NCEP Global Forecast System (GFS) Analyses

- and Forecasts. Research Data Archive at the National Center for Atmospheric Research, Computational and Information Systems Laboratory, College Park.
- [25] Parrish, D.F. and Derber, J.C. (1992) The National Meteorological Center's Spectral Statistical-Interpolation Analysis System. *Monthly Weather Review*, **120**, 1747-1763. [https://doi.org/10.1175/1520-0493\(1992\)120%3C1747:TNMCSS%3E2.0.CO;2](https://doi.org/10.1175/1520-0493(1992)120%3C1747:TNMCSS%3E2.0.CO;2)
- [26] Berre, L., Ștefănescu, S.E. and Pereira, M.B. (2006) The Representation of the Analysis Effect in Three Error Simulation Techniques. *Tellus A: Dynamic Meteorology and Oceanography*, **58**, 196-209. <https://doi.org/10.1111/j.1600-0870.2006.00165.x>
- [27] Chevallier, F. (2004) A One-Dimensional Variational Analysis Package. NWP SAF Report No. NWPSAF-EC-UD-001. European Centre for Medium-Range Weather Forecasts, Reading, United Kingdom. [https://nwpsaf.eu/site/download/documentation/ecmwf\\_1dvar/nwpsaf-ec-ud-001.pdf](https://nwpsaf.eu/site/download/documentation/ecmwf_1dvar/nwpsaf-ec-ud-001.pdf)
- [28] Weston, P. (2014) NWPSAF 1D-Var User Manual. Met Office Doc ID: NWPSAF-MO-UD-032, Met Office, Exeter. <https://nwpsaf.eu/site/download/documentation/1dvar/AppendixB.pdf>
- [29] Havemann, S. (2020) NWPSAF 1D-Var User Manual Software Version 1.2. AS Mission Report NWPSAF-MO-UD-032, EUMETSAT Numerical Weather Prediction Satellite Applications Facility, Darmstadt, Germany.
- [30] Sherlock, V. and Collard, A. (2005) A Simulation Study of the Impact of AIRS Fast Model Errors on the Accuracy of 1D-Var Retrievals from AIRS Radiances. *Proceedings of 14th International TOVS Study Conference*, Beijing, 25-31 May 2005, 647-654. [http://library.ssec.wisc.edu/research\\_Resources/publications/pdfs/ITSC14/sherlock02\\_ITSC14\\_2005.pdf](http://library.ssec.wisc.edu/research_Resources/publications/pdfs/ITSC14/sherlock02_ITSC14_2005.pdf)
- [31] Bauer, P., Lopez, P., Benedetti, A., Salmond, D. and Moreau, E. (2006) Implementation of 1D+4D-Var Assimilation of Precipitation-Affected Microwave Radiances at ECMWF. I: 1D-Var. *Quarterly Journal of the Royal Meteorological Society*, **132**, 2277-2306. <https://doi.org/10.1256/qj.05.189>
- [32] Geer, A.J., Migliorini, S. and Matricardi, M. (2019) All-Sky Assimilation of Infrared Radiances Sensitive to Mid- and Upper-Tropospheric Moisture and Cloud. *Atmospheric Measurement Techniques*, **12**, 4903-4929. <https://doi.org/10.5194/amt-12-4903-2019>
- [33] Coopmann, O., Guidard, V., Fourrié, N., Josse, B. and Marécal, V. (2020) Update of Infrared Atmospheric Sounding Interferometer (IASI) Channel Selection with Correlated Observation Errors for Numerical Weather Prediction (NWP). *Atmospheric Measurement Techniques*, **13**, 2659-2680. <https://doi.org/10.5194/amt-13-2659-2020>
- [34] McNally, A.P. (2009) The Direct Assimilation of Cloud-Affected Satellite Infrared Radiances in the ECMWF 4D-Var. *Quarterly Journal of the Royal Meteorological Society*, **135**, 1214-1229. <https://doi.org/10.1002/qj.426>
- [35] Pangaud, T., Fourrié, N., Guidard, V., Dahoui, M. and Rabier, F. (2009) Assimilation of AIRS Radiances Affected by Mid-to Low-Level Clouds. *Monthly Weather Review*, **137**, 4276-4292. <https://doi.org/10.1175/2009MWR3020.1>
- [36] Lavanant, L., Fourrié, N., Gambacorta, A., Grieco, G., Heilliette, S., Hilton, F.I., *et al.* (2011) Comparison of Cloud Products within IASI Footprints for the Assimilation of Cloudy Radiances. *Quarterly Journal of the Royal Meteorological Society*, **137**, 1988-2003. <https://doi.org/10.1002/qj.917>

- [37] Eyre, J.R. and Menzel, W.P. (1989) Retrieval of Cloud Parameters from Satellite Sounder Data: A Simulation Study. *Journal of Applied Meteorology and Climatology*, **28**, 267-275. [https://doi.org/10.1175/1520-0450\(1989\)028%3C0267:ROCPFS%3E2.0.CO;2](https://doi.org/10.1175/1520-0450(1989)028%3C0267:ROCPFS%3E2.0.CO;2)
- [38] Rodgers, C.D. (2000) Inverse Methods for Atmospheres: Theory and Practice. Vol. 2, World Scientific, Singapore. <https://doi.org/10.1142/3171>  
[https://library.wmo.int/doc\\_num.php?explnum\\_id=1654](https://library.wmo.int/doc_num.php?explnum_id=1654)
- [39] Lorenc, A.C. (1986) Analysis Methods for Numerical Weather Prediction. *Quarterly Journal of the Royal Meteorological Society*, **112**, 1177-1194. <https://doi.org/10.1002/qj.49711247414>
- [40] Courtier, P. (1997) Variational Methods. *Journal of the Meteorological Society of Japan*, **75**, 211-218.
- [41] Ide, K., Courtier, P., Ghil, M. and Lorenc, A.C. (1997) Unified Notation for Data Assimilation: Operational, Sequential and Variational. *Journal of the Meteorological Society of Japan*, **75**, 181-189.
- [42] Andersson, E., Haseler, J., Undén, P., Courtier, P., Kelly, G., Vasiljevic, D., *et al* (1998) The ECMWF Implementation of Three-Dimensional Variational Assimilation (3D-Var). III: Experimental Results. *Quarterly Journal of the Royal Meteorological Society*, **124**, 1831-1860. <https://doi.org/10.1002/qj.49712455004>
- [43] Havemann, S., Thelen, J.C., Taylor, J.P. and Keil, A. (2009) The Havemann-Taylor Fast Radiative Transfer Code: Exact Fast Radiative Transfer for Scattering Atmospheres Using Principal Components (PCs). *AIP Conference Proceedings*, **1100**, 38-40. <https://doi.org/10.1063/1.3117000>
- [44] Havemann, S., Thelen, J.C., Taylor, J.P. and Harlow, R.C. (2018) The Havemann-Taylor Fast Radiative Transfer Code (HT-FRTC): A Multipurpose Code Based on Principal Components. *Journal of Quantitative Spectroscopy and Radiative Transfer*, **220**, 180-192. <https://doi.org/10.1016/j.jqsrt.2018.09.008>
- [45] Saunders, R., Matricardi, M. and Brunel, P. (1999) A Fast Radiative Transfer Model for Assimilation of Satellite Radiance Observations-RTTOV-5. European Centre for Medium-Range Weather Forecasts, Reading. <https://nwpsaf.eu/oldsite/deliverables/rtm/papers/tm282.pdf>
- [46] Saunders, R., Hocking, J., Turner, E., Rayer, P., Rundle, D., Brunel, P., *et al* (2018) An Update on the RTTOV Fast Radiative Transfer Model (Currently at Version 12). *Geoscientific Model Development*, **11**, 2717-2737. <https://doi.org/10.5194/gmd-11-2717-2018>
- [47] Weng, F., Han, Y., van Delst, P., Liu, Q. and Yan, B. (2010) JCSDA Community Radiative Transfer Model (CRTM). *14th International TOVS Study Conference*, Monterey, 14-20 April 2010, 217-222. [http://cimss.ssec.wisc.edu/itwg/itsc/itsc17/session4/4.5\\_y\\_han.pdf](http://cimss.ssec.wisc.edu/itwg/itsc/itsc17/session4/4.5_y_han.pdf)
- [48] Aumann, H.H., Chen, X., Fishbein, E., Geer, A., Havemann, S., Huang, X., *et al* (2018) Evaluation of Radiative Transfer Models with Clouds. *Journal of Geophysical Research: Atmospheres*, **123**, 6142-6157. <https://doi.org/10.1029/2017JD028063>
- [49] Li, W. and Wang, W. (2015) Study on Channel Selection Evaluation Model of Painting Material Industry Based on Brand Building. *Open Journal of Business and Management*, **3**, 425-432. <https://doi.org/10.4236/ojbm.2015.34042>
- [50] Siméoni, D., Singer, C. and Chalon, G. (1997) Infrared Atmospheric Sounding Interferometer. *Acta Astronautica*, **40**, 113-118. [https://doi.org/10.1016/S0094-5765\(97\)00098-2](https://doi.org/10.1016/S0094-5765(97)00098-2)
- [51] Glumb, R.J., Williams, F.L., Funk, N., Chateaufneuf, F., Roney, A. and Allard, R.

- (2003, November) Cross-Track Infrared Sounder (CrIS) Development Status. *Optical Science and Technology SPIE's 48th Annual Meeting*, Vol. 5152, San Diego, 3-8 August 2003, 1-8. <https://doi.org/10.1117/12.508544>
- [52] Timofeyev, Y.M., Uspensky, A. B., Zavelevich, F. S., Polyakov, A. V., Virolainen, Y. A., Rublev, A. N., *et al.* (2019) Hyperspectral Infrared Atmospheric Sounder IKFS-2 on “Meteor-M” No. 2—Four Years in Orbit. *Journal of Quantitative Spectroscopy and Radiative Transfer*, **238**, Article ID: 106579. <https://doi.org/10.1016/j.jqsrt.2019.106579>
- [53] Qi, C., Wu, C., Hu, X., Xu, H., Lee, L., Zhou, F., *et al.* (2020) High Spectral Infrared Atmospheric Sounder (HIRAS): System Overview and On-Orbit Performance Assessment. *IEEE Transactions on Geoscience and Remote Sensing*, **58**, 4335-4352. <https://doi.org/10.1109/TGRS.2019.2963085>
- [54] Eresmaa, R. (2021) Infrared Fourier Spectrometer 2 (IKFS-2) Radiance Assimilation at ECMWF. *Quarterly Journal of the Royal Meteorological Society*, **147**, 106-120. <https://doi.org/10.1002/qj.3908>
- [55] National Centers for Environmental Prediction/National Weather Service/NOAA/U.S. Department of Commerce (2008) NCEP ADP Global Upper Air and Surface Weather Observations (PREPBUFR Format). Research Data Archive at the National Center for Atmospheric Research, Computational and Information Systems Laboratory, Boulder.
- [56] Lavanant, L., Dahoui, M., Rabier, F. and Auligné, T. (2004) Cloud Detection for IASI/AIRS Using Imagery. Workshop on Assimilation of High Spectral Resolution Sounders in NWP, Reading, 28 June-1 July 2004, 133-144. <https://www.ecmwf.int/sites/default/files/elibrary/2004/10663-cloud-detection-iasiairs-using-imagery.pdf>
- [57] Matricardi, M. (2008) The Generation of RTTOV Regression Coefficients for IASI and AIRS Using a New Profile Training Set and a New Line-by-Line Database. European Centre for Medium-Range Weather Forecasts, Reading. <https://www.ecmwf.int/sites/default/files/elibrary/2008/11040-generation-rttov-regression-coefficients-iasi-and-airis-using-new-profile-training-set-and-new.pdf>